A highly stable zinc-air battery based on a non-alkaline agar gel electrolyte

Pengfei Zhang[a], Xinjie Li[a], Ziyue Li[a], Jiayun Zhang[a], Qian Wen[a,b], Runjing Xu[a], Jinyu Yang[a], Mingxu Wang[a], Chaoxin Wu[a], Fengmei Wang[a], Ya Zhang[b], Zihao Zhang[a], Dalin Sun[a], Fang Fang[a], Qian Cheng[b*], Fei Wang[a]*

[a]College of Smart Materials and Future Energy, Fudan University, Shanghai 200433, China

[b]Hefei Gotion High-Tech Power Energy Co., Hefei, Anhui, 230011, China

*Corresponding author: Qian Cheng, Email: q.cheng@gotion.com
Fei Wang, E-mail: feiw@fudan.edu.cn

Methods

Materials

Agar (Sinopharm Chemical Reagent Co., Ltd.), Zinc trifluoromethanesulfonate ($Zn(OTf)_2$, 99.5%, Jiangxi Guohua Pharmaceutical Technology Co., Ltd.), Deionized water, Carbon powder (Cabot, XC-72R, Suzhou Shengernuo Technology Co., Ltd.), Polytetrafluoroethylene (PTFE, Aladdin), Glass fiber (Whatman GF/A), Potassium hydroxide (KOH, AR, ≥85%, Aladdin), Ethanol (C_2H_6O, AR, 95%, Sinopharm Chemical Reagent Co., Ltd.), Zn foil (0.03 mm thick, Hefei Wenghe Metal Materials Co., Ltd.), Sn foil (0.03 mm thick, Hefei Wenghe Metal Materials Co., Ltd.), Cu foil (0.05 mm thick, Hefei Wenghe Metal Materials Co., Ltd.), Cu mesh (20-mesh 0.05mm thick, Xingtai Metal Materials Co., Ltd.), Ti mesh (200-mesh, 0.2mm thick, Xingtai Metal Materials Co., Ltd.)

Synthesis of the AG electrolyte

1.0 g of agar powder was added to 20 mL 0.3 M $Zn(OTf)_2$ solution, and then magnetically stirred at 120 ℃ for 10 min. Then adjust the temperature to 100 ℃ and continue stirring for 5 min to ensure that the mixed solution forms a uniform and bubble-free slurry. The heated agar electrolyte precursor was injected into a polytetrafluoroethylene mold with a diameter of 1.2 cm and a depth of 2 mm by using a pipette. After natural cooling, use a small knife to cut off the excess gel electrolyte along the top of the mold, and finally peel it out of the mold to obtain the AG electrolyte.

Synthesis of the AG polymer

The preparation process of AG polymer can refer to AG electrolyte. The zinc salt solution is replaced with deionized water, and the other processes are consistent with the preparation of AG electrolyte.

Preparation of the Air Cathode

Carbon powder and PTFE were mixed in a mass ratio of 9:1, and prepared a mixed slurry with ethanol. To achieve better uniform dispersion, the slurry was ultrasonically treated for 30 min and then placed in an oven at 60 ℃ to remove the excess ethanol. The obtained mixture was kneaded into a dough-like shape, and then repeatedly rolled with a roller press to obtain a 0.5 mm thick film. The prepared carbon film was baked at 60 ℃ for 12 h to further remove ethanol. Then it was cut into circular pieces with a diameter of 12 mm, and finally rolled onto a Ti mesh as an air electrode. All the air cathodes used in this work were prepared by this method. Except for the differences in shape and size, the material, texture and thickness of the air cathode in all types of zinc-air batteries remain consistent.

Assembly of Zn-based half battery

All the used zinc and Cu electrodes in experiment were polished by 1000-mesh fine sandpaper (Eagle brand) before use, this operation is also employed in the construction of the full batteries. The polished zinc foil and Cu foil were directly used as electrodes for symmetrical and asymmetric batteries, with an exposed effective reaction area of 1.0 cm×1.0 cm. Liquid AG electrolyte was poured between two zinc electrodes, the Zn||Zn symmetrical battery can be directly obtained after cooling and curing. Zn||Cu asymmetric battery was assembled according to the similar method as described above.

Assembly of Zn-Air Battery

The zinc anode (12 mm) was placed at the bottom of the circular groove (2.1 mm thick, 12 mm in diameter), and press it flat with a steel sheet of the same diameter. Liquid AG electrolyte was injected into the space of the groove. After slight cooling, the air cathode was placed at the top. Then press it flat with a glass plate until it cools and solidifies. Peel off the assembled sandwich type battery from the mold and then assemble it into a Swagelock zinc-air battery. A Sn foil (12 mm in diameter) was used as the current collector for the zinc anode. In the comparative experiment, glass fiber (Whatman GF/A, 13 mm in diameter) was used instead of AG electrolyte. The electrolyte solution used 0.3 M $Zn(OTf)_2$ or 6 M KOH. The corresponding current collectors in the liquid battery system are Sn foil (non-alkaline) and Cu foil (alkaline), respectively.

Assembly of pouch battery

The pouch zinc-air full battery is assembled from zinc electrodes, AG electrolyte and air electrodes (4.0×5.0 cm^2). The zinc foil is wrapped in Cu mesh to achieve better contact while serving as a current collector. Add a membrane between the zinc electrode and the air electrode to prevent short circuits and buffer the contact between the electrolyte and the electrode. Several holes need to be drilled in the sealing membrane on the air electrode side to connect with the atmosphere and ensure the normal operation of the battery. The AG electrolyte is filled into the assembled pouch battery, and then sealed to obtain the pouch zinc-air full battery. When assembling the liquid electrolyte-based zinc-air pouch battery, the two GF/A separators are placed on either side of the Cu mesh that wraps the zinc foil. The rest of the process is the same as constructing the AG-type pouch battery.

Characterizations

The ionic conductivity (σ) of the liquid electrolyte was measured at room temperature using the conductivity meter (DDSJ-307F, Shanghai Yidian Scientific Instrument Co., Ltd.). To obtain the ionic conductivity of the AG electrolyte, the electrochemical impedance spectroscopy of the assembled stainless steel sheet||AG electrolyte||stainless steel sheet battery (diameter: 1.2 cm) was tested using an electrochemical workstation (Shanghai Chenhua Instrument Co., Ltd.), with an amplitude of 5 mV and a frequency range of 100 kHz to 1 Hz. The ionic conductivity of AG gel electrolyte is calculated by the following formula:

$$\sigma = h/R \cdot A$$

where h represents the distance between the two stainless steel electrodes, A is the effective contact area between the AG electrolyte and the stainless steel electrode, and R is the intersection point value of the electrochemical curve with the horizontal axis.

The mechanical tolerance of AG electrolyte was evaluated through load experiments using standard weights. The FTIR data were obtained utilizing the Fourier Transform Infrared Spectrometer (Thermo Fisher Nicolet Is5). The Raman spectra of the sample was detected via Raman tester (LabRAM HR Evolution) with a laser wavelength of 532 nm. The XPS and XRD data were tested by the X-ray photoelectron spectrometer (Thermo Fisher K-ALPHA) and the X-ray diffractometer (Rigaku Ultima IV), respectively. The morphology and roughness of the electrode were observed and obtained by scanning electron microscopy (GeminiSEM 300) and confocal microscopy (CLSM, OLS-100).

Electrochemical measurements

The electrochemical stability windows (ESW) of different electrolytes were investigated through linear scanning voltammetry (LSV) tests. Tafel tests were conducted using the Zn||Zn battery on the CHI760E electrochemical workstation with a scan rate of 5 mV s^{-1}. Moreover, cyclic voltammetry (CV) and chronoamperometry (CA) tests were also carried out through the electrochemical workstation.

The galvanostatic charge-discharge tests of the batteries were all conducted on the LAND battery testing system (Wuhan, China), including the Zn||Zn symmetric battery, the Zn||Cu asymmetric battery, and the zinc-air full battery. Cyclic charge-discharge tests were conducted on the Zn||Zn symmetric battery at 1.0 mA cm^{-2} (1.0 mAh cm^{-2}) and 5.0 mA cm^{-2} (5.0 mAh cm^{-2}). The Zn||Cu asymmetric battery was subjected to charge-discharge cycle experiment of 1.0 mA cm^{-2} (1.0 mAh cm^{-2}), with the upper cutoff voltage of 0.5 V. In addition, discharge and cycling performance tests were performed on zinc-air battery at different current densities. The round-trip energy efficiency of zinc-air batteries is calculated via dividing the discharge voltage by the charge voltage. The discharge specific capacity of the zinc-air battery is calculated based on the total discharge capacity and the mass of the zinc electrode. All the experiments mentioned above were conducted at room temperature.

DFT calculation

Density functional theory (DFT) calculations were performed using the Gaussian 09 software based on the ab-initio first-principles calculation method. All the simulation models are constructed based on actual conditions, taking into account the presence of Zn^{2+}, H_2O, and with or without agar molecules. The truncation value of the kinetic energy of the electron wave function was set to 500 eV during the calculation process. The B3LYP-D3(BJ) functional and basis set of def2-SVP for all atoms were used for geometry optimizations and frequency calculations. Frequency outcomes were examined to confirm the stationary points as minima (no imaginary frequencies). Single-point energies were then calculated with B3LYP-D3(BJ) functional and def2-TZVP basis set for all atoms.

Supplementary Figure S1

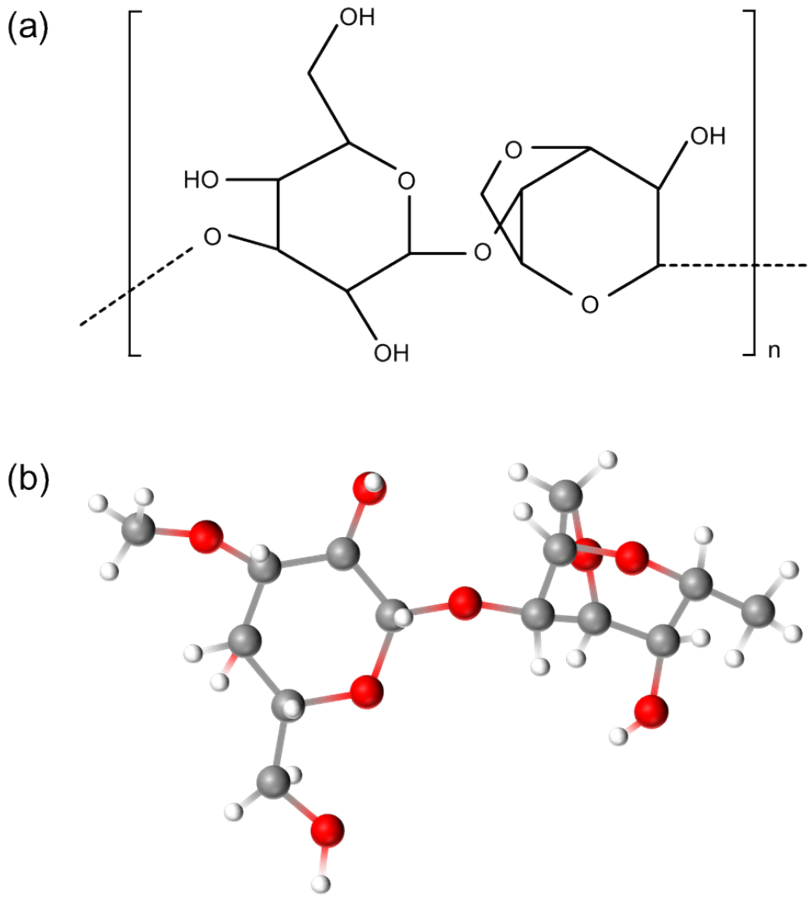

Supplementary Figure S1. Molecular structure (a) and model diagram (b) of the Agar.

Supplementary Figure S2

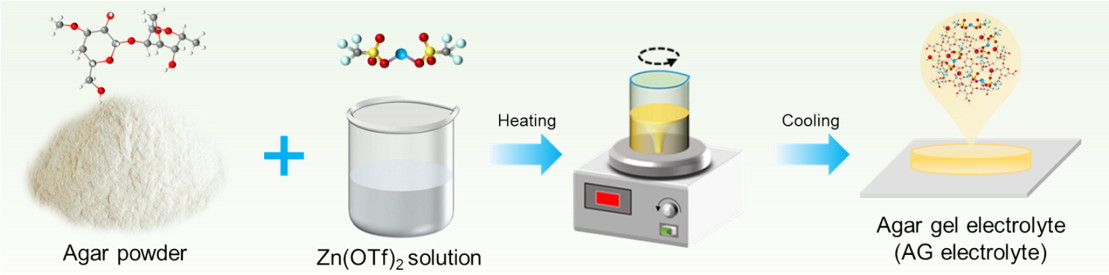

Supplementary Figure S2. Schematic diagram of the preparation process of AG electrolyte.

Supplementary Figure S3

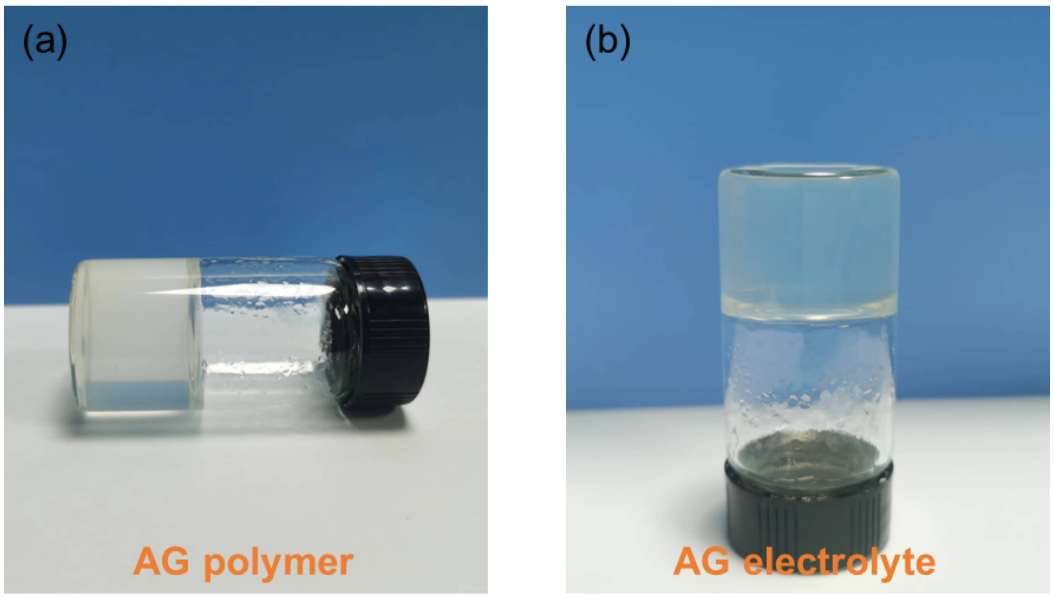

Supplementary Figure S3. Optical photos of AG polymer (a) and AG electrolyte (b).

Supplementary Figure S4

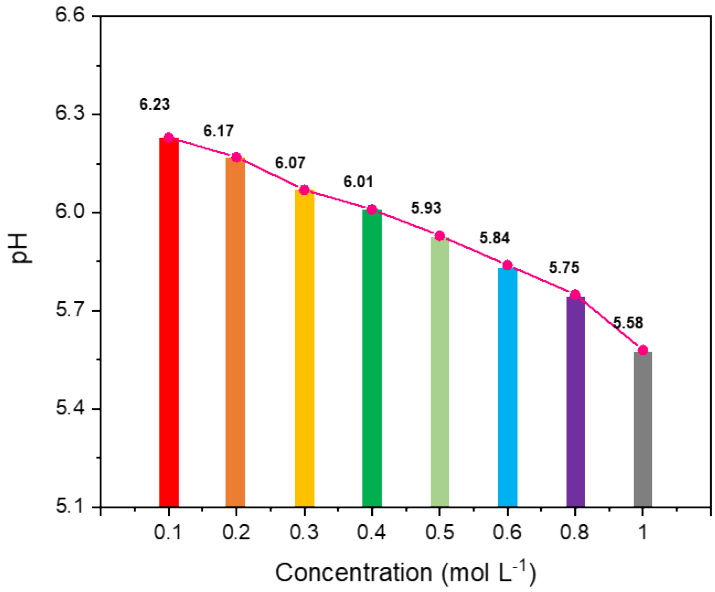

Supplementary Figure S4. The pH values of $Zn(OTf)_2$ solutions with different concentrations (0.1, 0.2, 0.3, 0.5, 0.6, 0.8, 1.0 mol L^{-1}).

Supplementary Figure S5

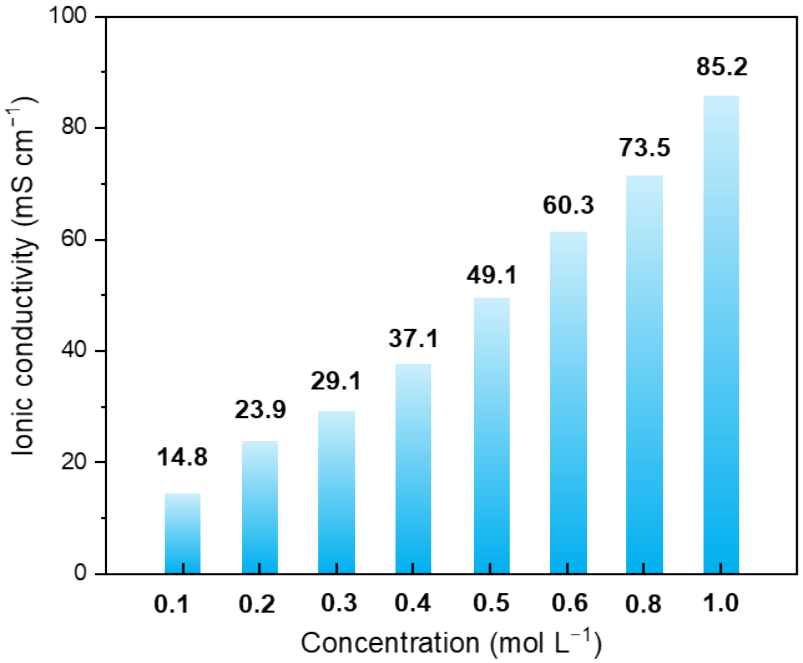

Supplementary Figure S5. Ionic conductivities of $Zn(OTf)_2$ solutions with different concentrations (0.1, 0.2, 0.3, 0.5, 0.6, 0.8, 1.0 mol L^{-1}).

Supplementary Figure S6

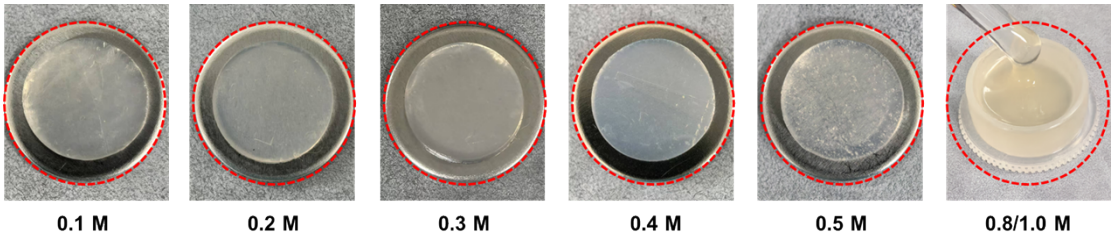

Supplementary Figure S6. Optical images of AG electrolyte synthesized from $Zn(OTf)_2$ solutions of different concentrations.

Supplementary Figure S7

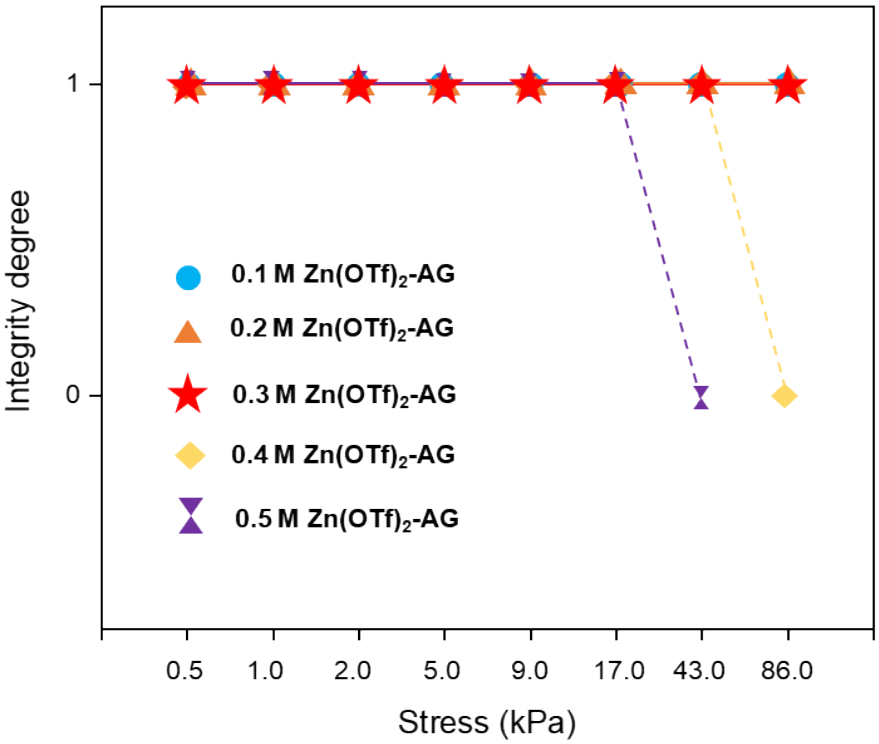

Supplementary Figure S7. Comparison of the mechanical properties of AG electrolytes synthesized from $Zn(OTf)_2$ solutions of different concentrations (1 indicates completeness, 0 indicates rupture).

Supplementary Figure S8

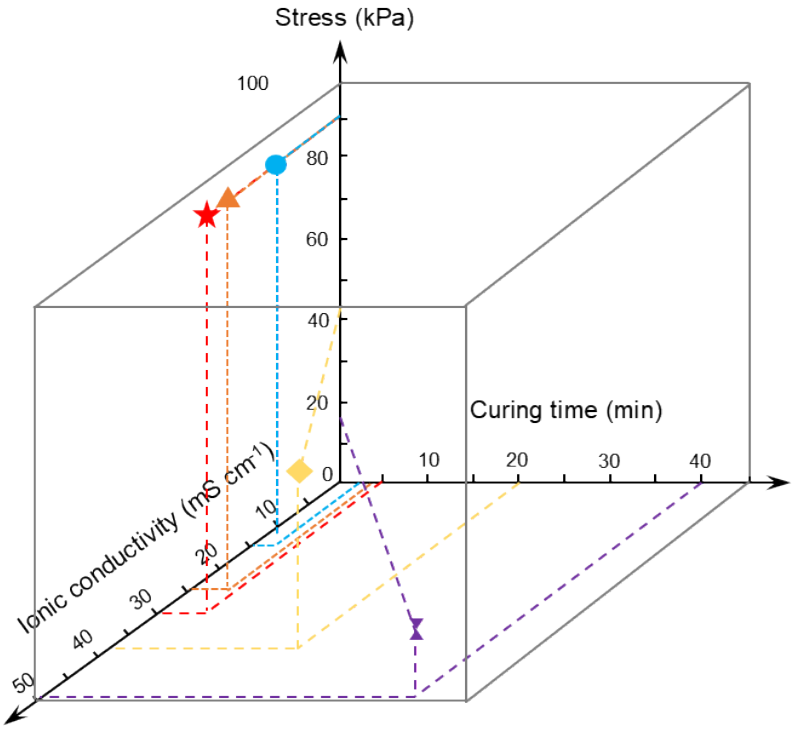

Supplementary Figure S8. The selection criteria for the 0.3 M-AG electrolyte in this work.

Supplementary Figure S9

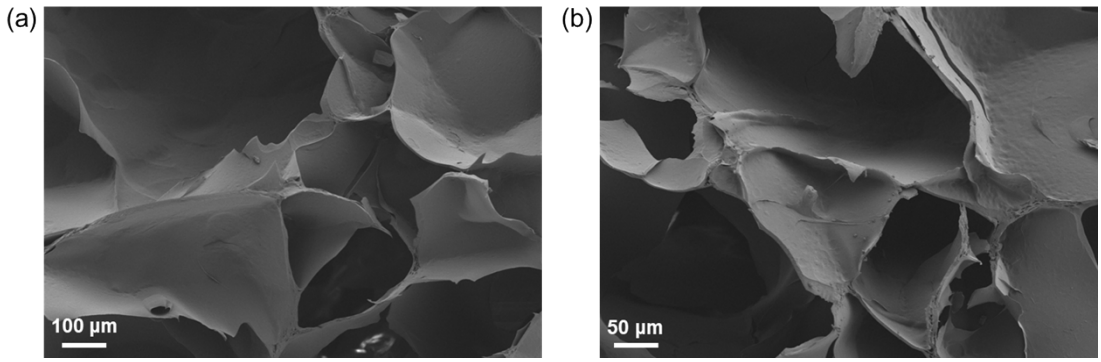

Supplementary Figure S9. SEM images of AG electrolyte at the scales of 100 μm (a) and 50 μm (b).

Supplementary Figure S10

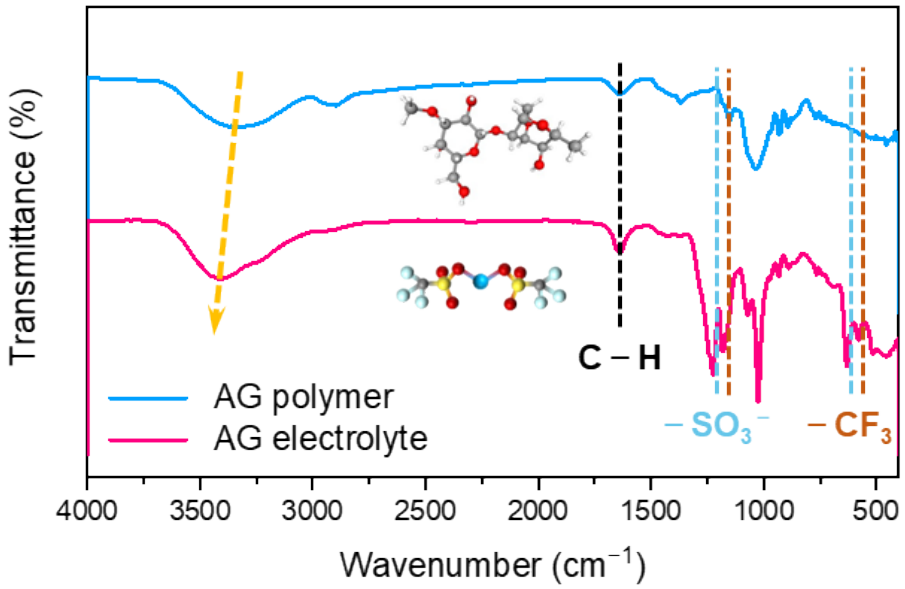

Supplementary Figure S10. FT-IR spectrum of AG polymer and AG electrolyte.

Supplementary Figure S11

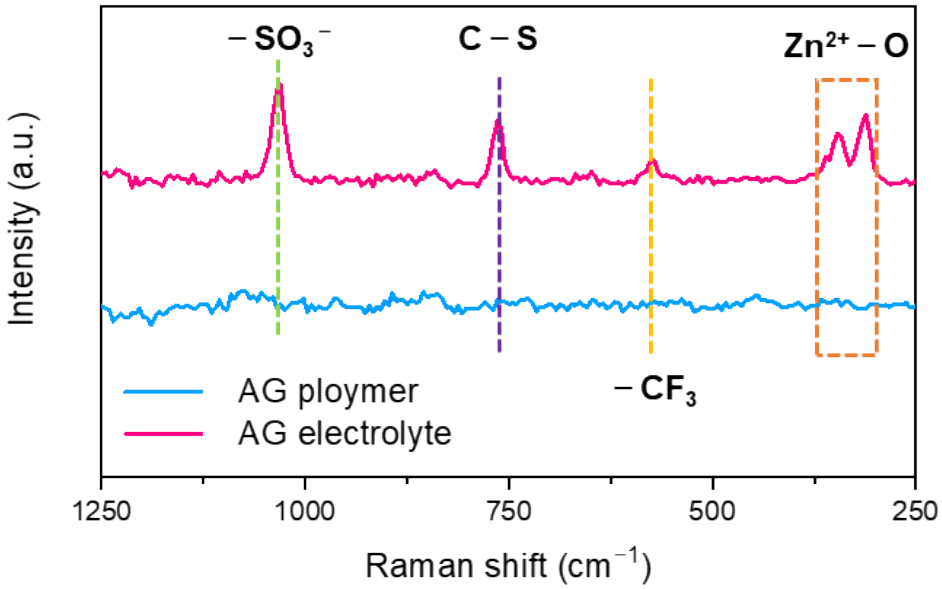

Supplementary Figure S11. Raman spectrum of AG polymer and AG electrolyte.

Supplementary Figure S12

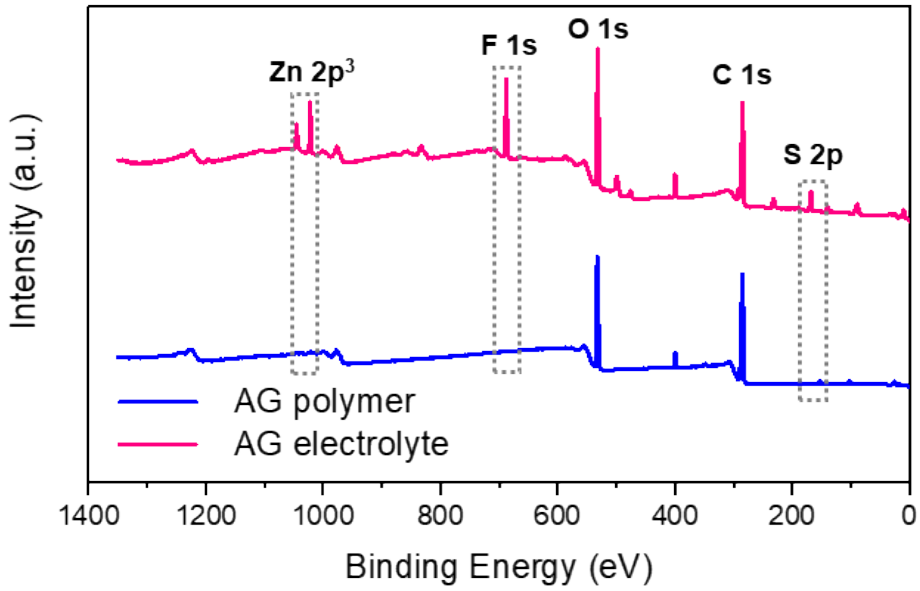

Supplementary Figure S12. XRS spectrum of AG polymer and AG electrolyte.

Supplementary Figure S13

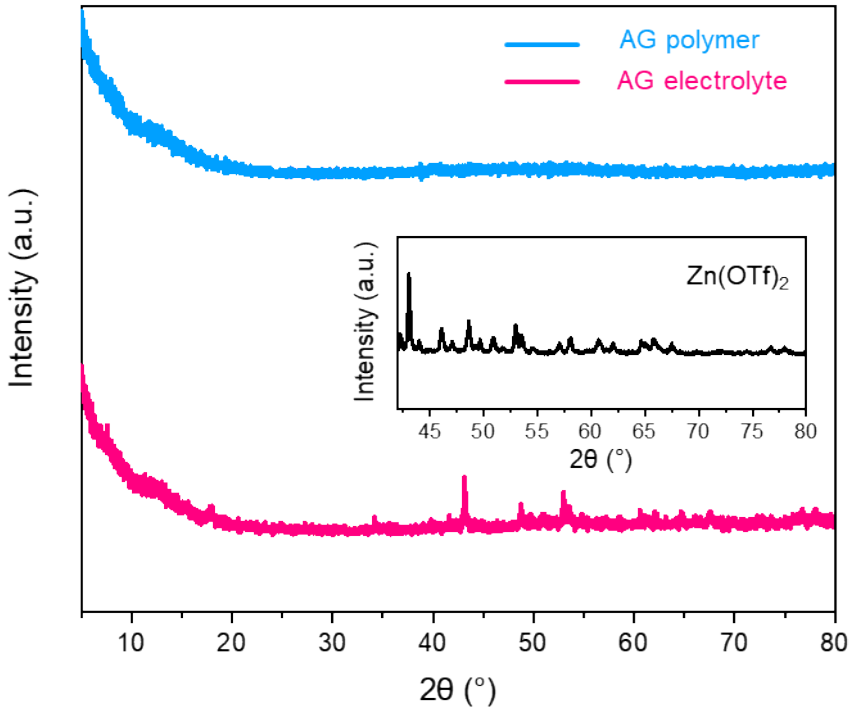

Supplementary Figure S13. XRD patterns of AG polymer and AG electrolyte (Inset shows the XRD pattern of $Zn(OTf)_2$ powder).

Supplementary Figure S14

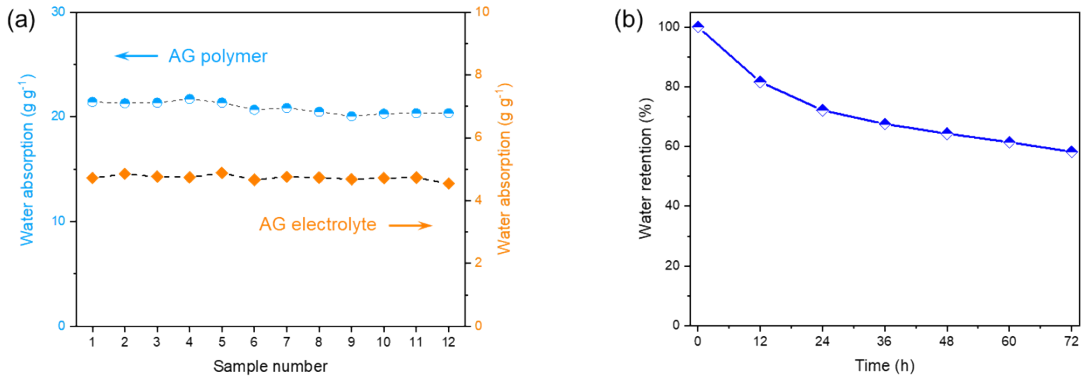

Supplementary Figure S14. (a) Water absorption of AG polymer and AG electrolyte. (b) Water retention of AG electrolyte.

Supplementary Figure S15

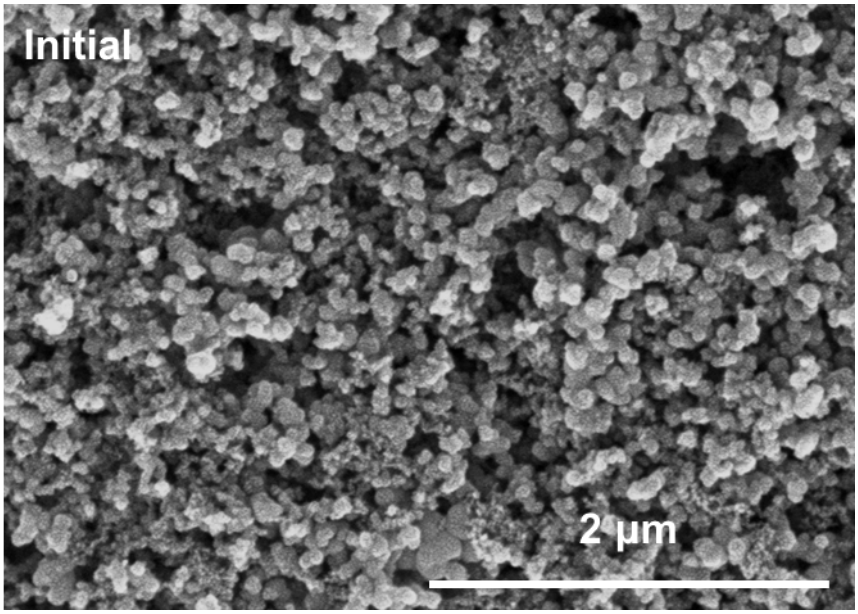

Supplementary Figure S15. SEM image of initial air cathode.

Supplementary Figure S16

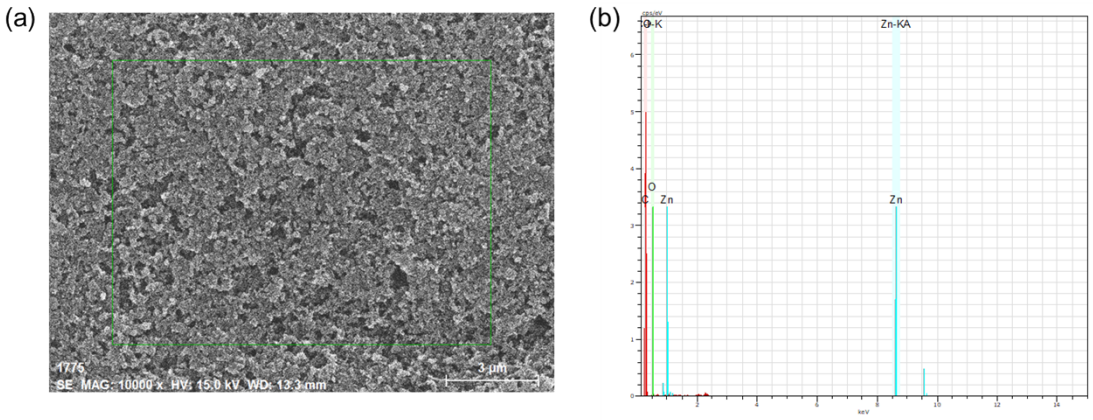

Supplementary Figure S16. (a) SEM image of the air cathode in full discharged state and (b) the corresponding elemental analysis diagram.

Supplementary Figure S17

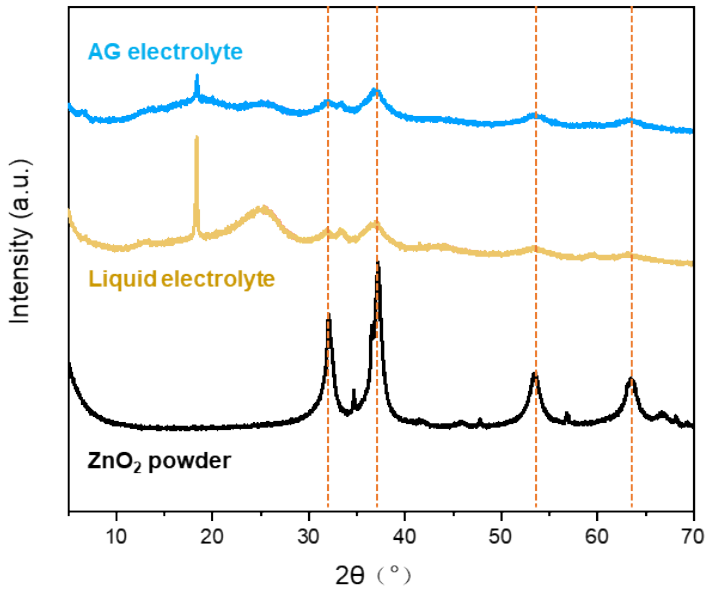

Supplementary Figure S17. XRD patterns of the AG/liquid electrolyte air cathode and ZnO_2 powder.

Supplementary Figure S18

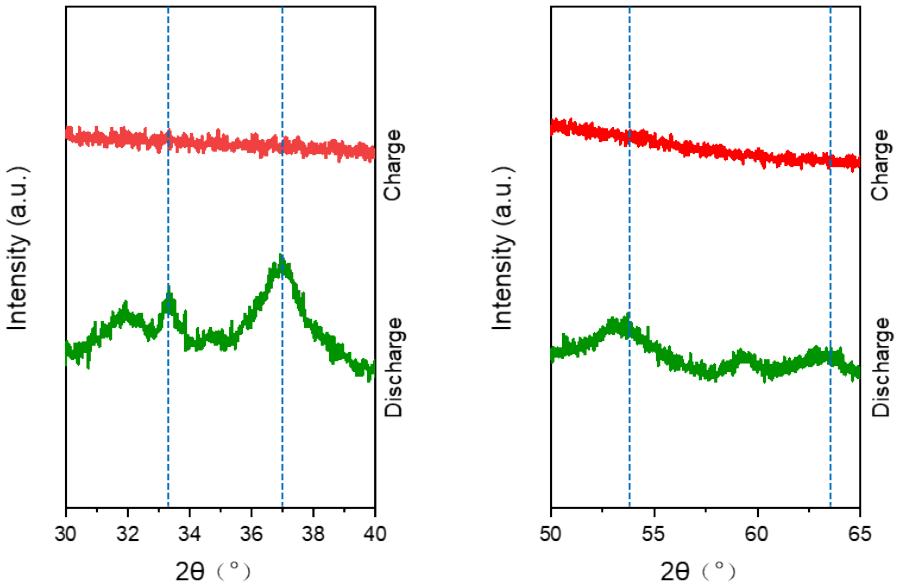

Supplementary Figure S18. XRD patterns of the air cathode in the AG electrolyte system after discharge and charging.

Supplementary Figure S19

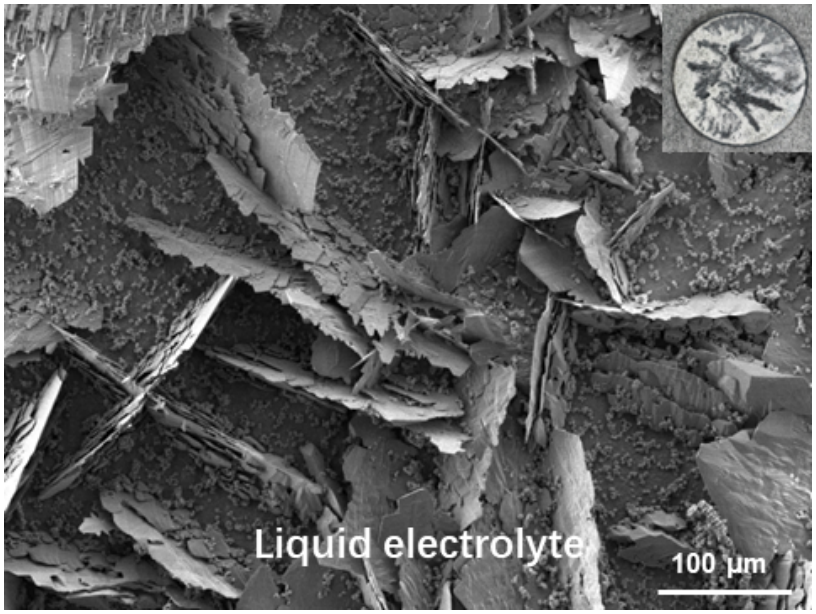

Supplementary Figure S19. SEM image and Optical photo of soaked Zn anode in liquid electrolyte for 15 days.

Supplementary Figure S20

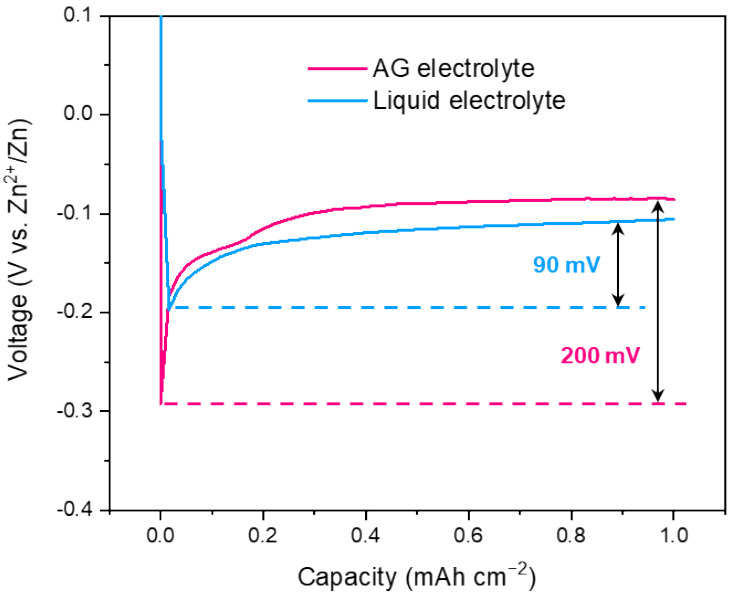

Supplementary Figure S20. Nucleation overpotential observed on Zn||Cu battery at a current density of 1.0 mA cm^{-2}.

Supplementary Figure S21

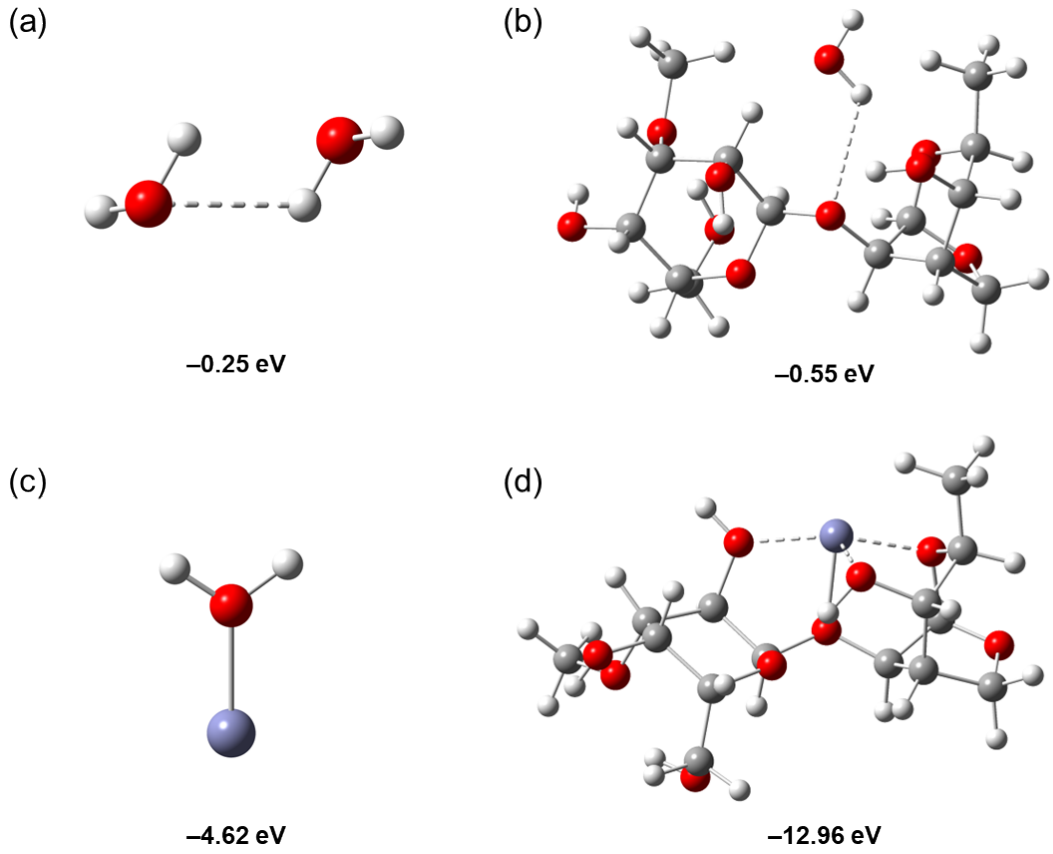

Supplementary Figure S21. The binding energy and molecular structure model: (a) H_2O–H_2O, (b) H_2O–AG, (c) H_2O–Zn^{2+}, (d) AG–Zn^{2+}.

Supplementary Figure S22

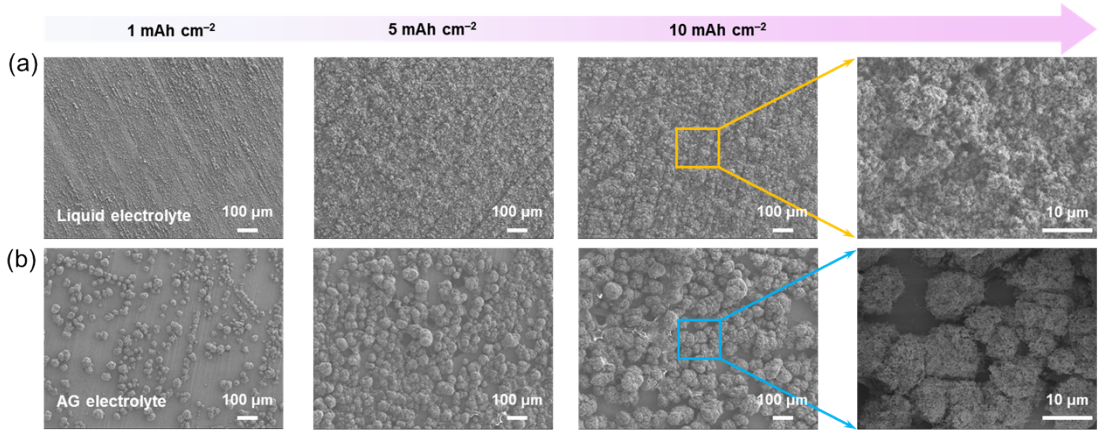

Supplementary Figure S22. SEM images of zinc deposition at a constant current density of 1.0 mA cm^{-2} with different areal capacities in liquid electrolyte (a) and AG electrolyte (b).

Supplementary Figure S23

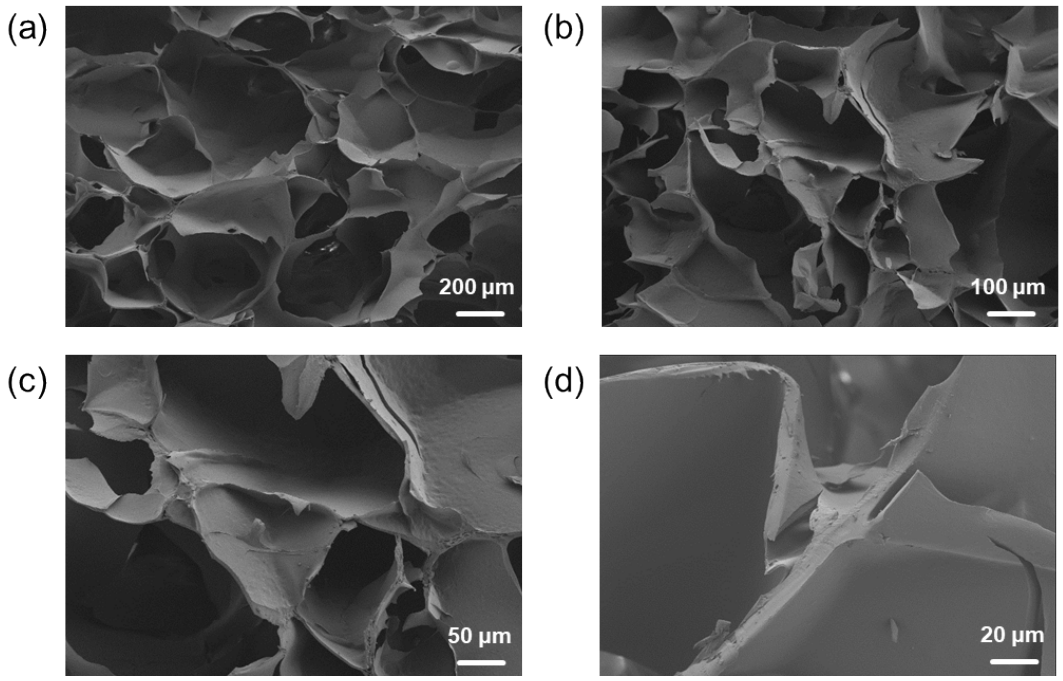

Supplementary Figure S23. Ion transport channels in SEM images of AG electrolyte at 200 μm (a), 100 μm (b), 50 μm (c), 20 μm (d).

Supplementary Figure S24

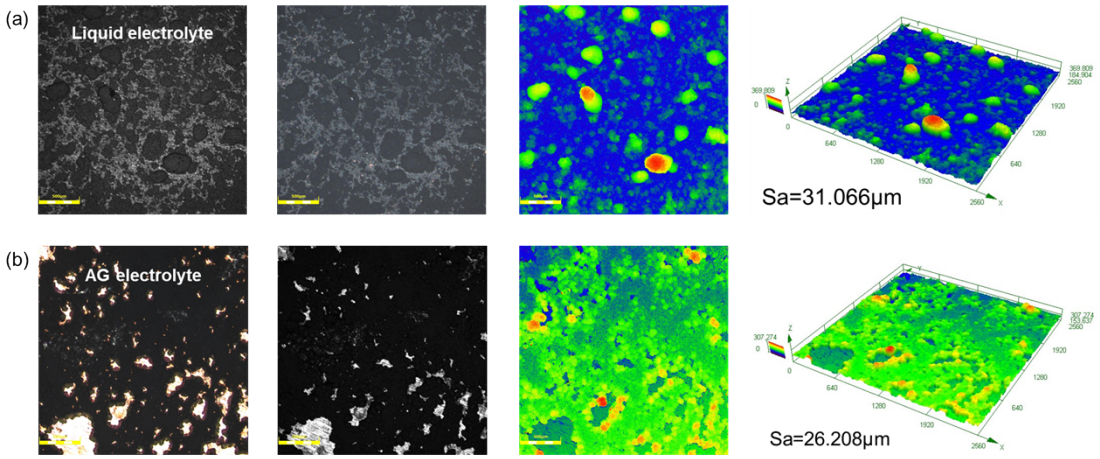

Supplementary Figure S24. Three-dimensional confocal laser microscopy images of Zn plating on Cu current collectors with a capacity of 10.0 mAh cm^{-2} in liquid electrolyte (a) and AG electrolyte (b). (Sa arithmetic mean height).

Supplementary Figure S25

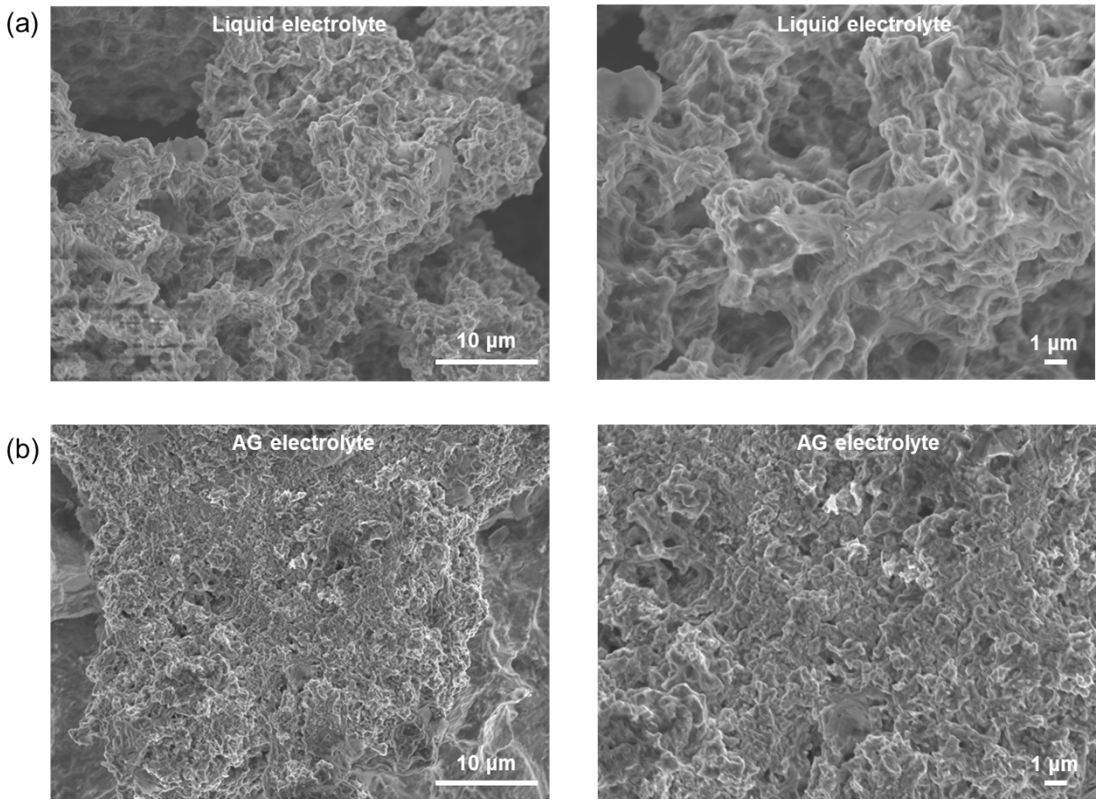

Supplementary Figure S25. SEM images of zinc electrode after 100 h of cycling in Zn||Zn symmetric battery based on liquid electrolyte (a) and AG electrolyte (b).

Supplementary Figure S26

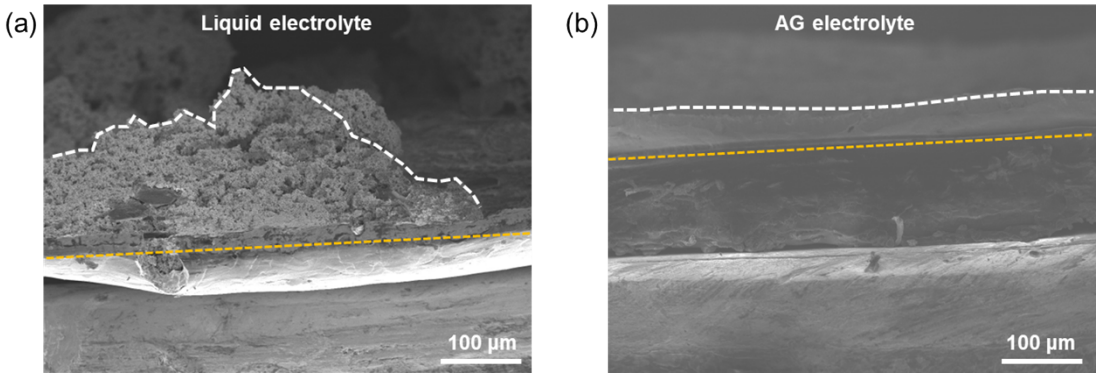

Supplementary Figure S26. Cross-section SEM images of Zn electrode after 100 h cycles in liquid electrolyte (a) and AG electrolyte (b).

Supplementary Figure S27

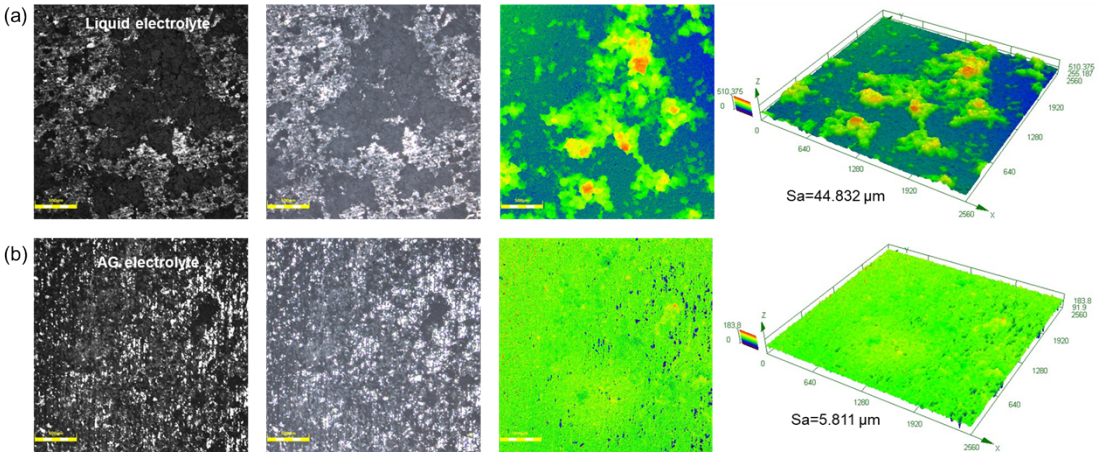

Supplementary Figure S27. Three-dimensional confocal laser microscopy images of Zn electrode in Zn||Zn symmetric battery after 100 h cycles with liquid electrolyte (a) and AG electrolyte (b). (Sa arithmetic mean height).

Supplementary Figure S28

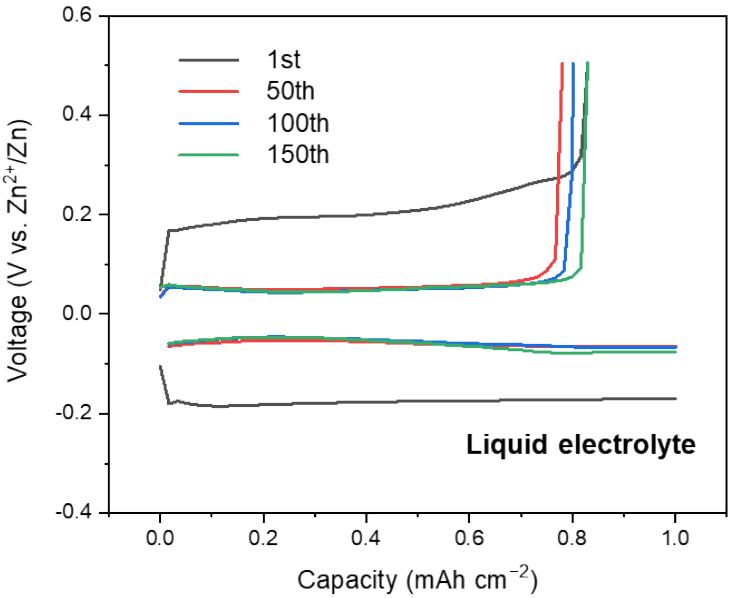

Supplementary Figure S28. Galvanostatic voltage profiles of the Zn||Cu asymmetric battery with AG electrolyte.

Supplementary Figure S29

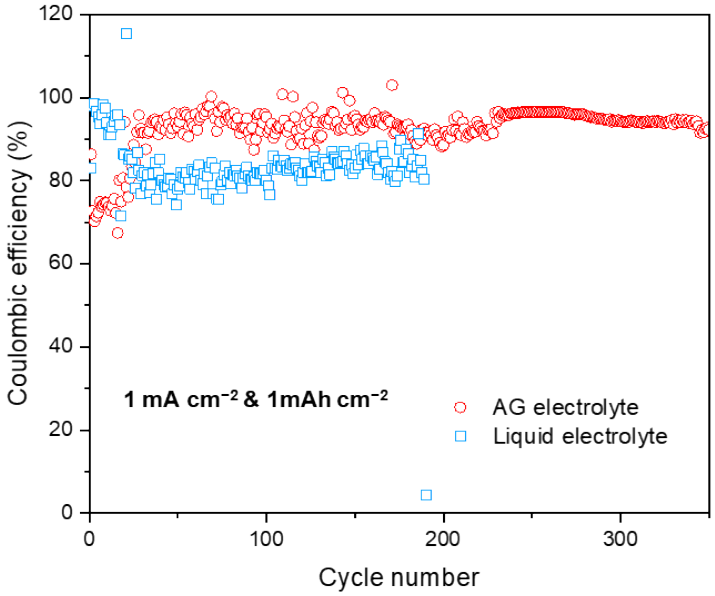

Supplementary Figure S29. CE values of Zn electroplating-stripping in liquid and AG-based Zn||Cu asymmetric battery at 1.0 mA cm^{-2} with a capacity of 1.0 mAh cm^{-2}.

Supplementary Figure S30

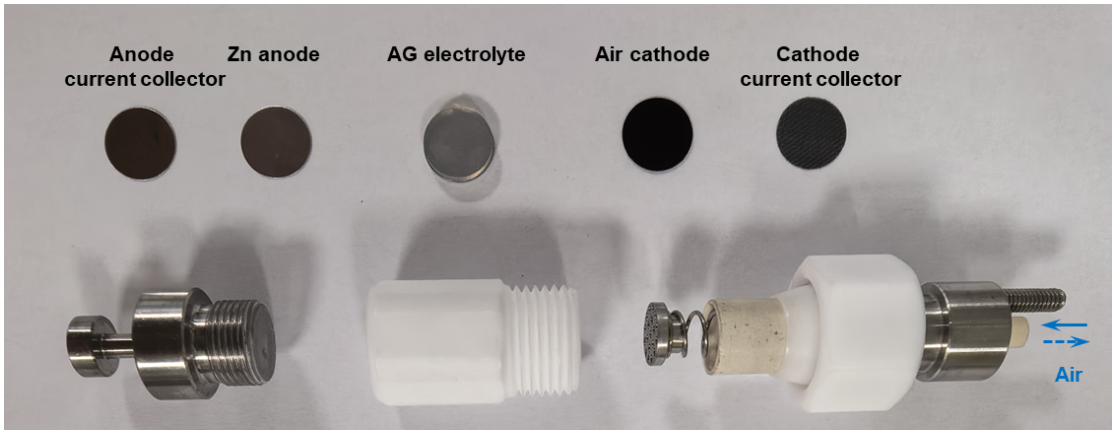

Supplementary Figure S30. The structural composition of the Swagelok mold battery assembled using AG electrolyte.

Supplementary Figure S31

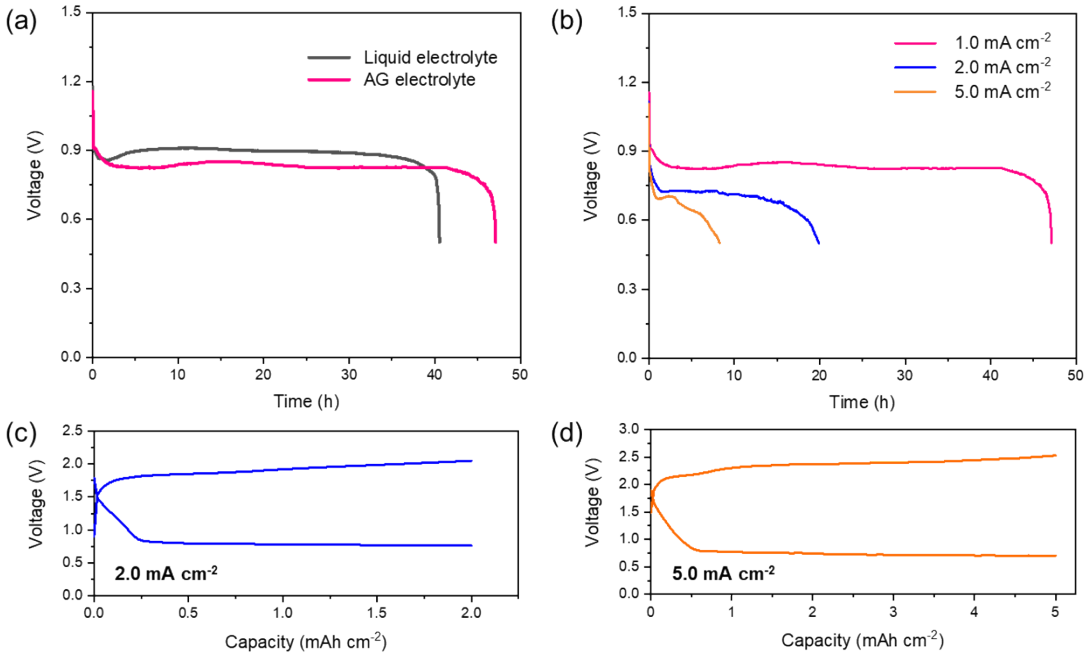

Supplementary Figure S31. (a) Galvanostatic discharge duration of zinc-air batteries with liquid and AG electrolytes at 1.0 mA cm^{-2} (cutoff voltage: 0.5 V). (b) Galvanostatic discharge duration of zinc-air batteries with AG electrolyte at 1.0, 2.0 and 5.0 mA cm^{-2} (cutoff voltage: 0.5 V). The charge-discharge polarization curve at the current density of 2.0 mA cm^{-2} (c) and 5.0 mA cm^{-2} (d).

Supplementary Figure S32

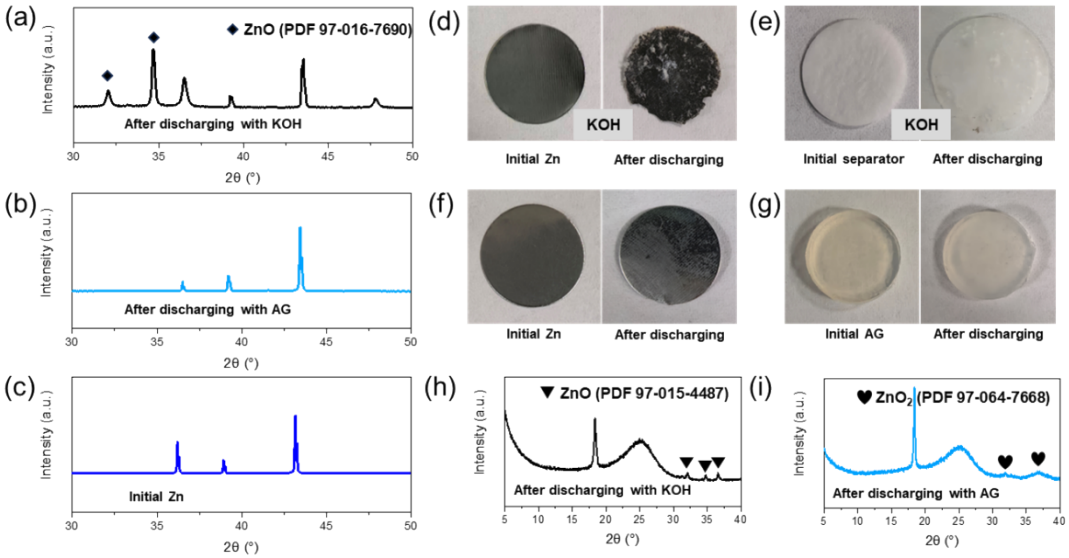

Supplementary Figure S32. The XRD spectra of the zinc electrode after 5 h of discharge in the KOH system (a) and the AG electrolyte system (b). (c) XRD spectra of initial Zn foil. Optical images comparison of the zinc electrode (d) and GF/A separator (e) before and after discharge in the KOH system. Optical images comparison of the zinc electrode (f) and gel electrolyte (g) before and after discharge in AG system. The XRD spectra of the air electrode after 5 h of discharge in the KOH system (h) and the AG electrolyte system (i).

Supplementary Figure S33

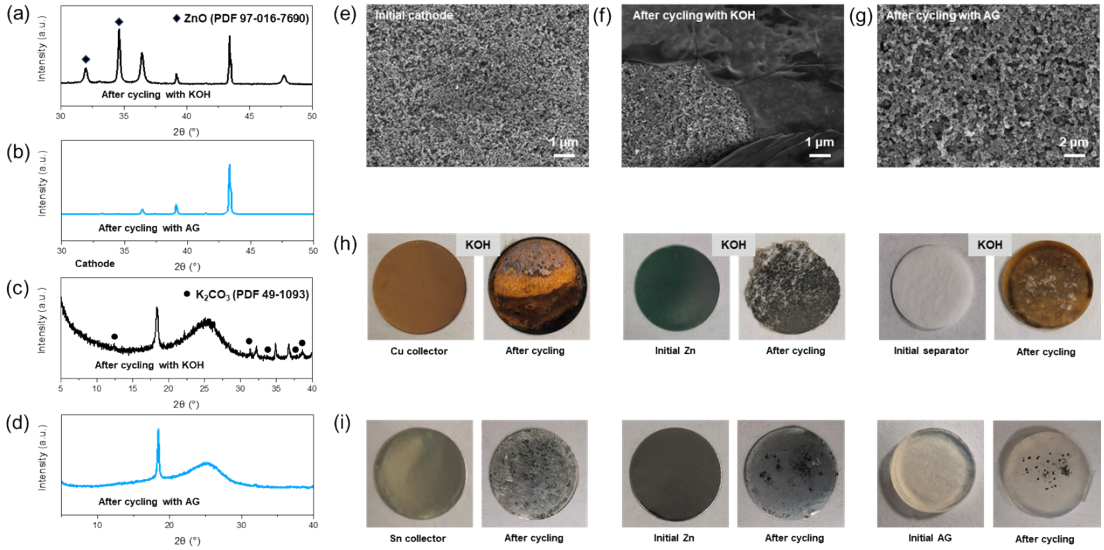

Supplementary Figure S33. The XRD spectra of the zinc electrode after 2 cycles in the KOH system (a) and the AG electrolyte system (b). The XRD spectra of the air electrode after 2 cycles in the KOH system (c) and the AG electrolyte system (d). (e) SEM image of initial air electrode. SEM images comparison of the air electrode before and after cycling in the KOH system(f) and AG electrolyte (g). (h) Optical image comparison of the Cu collector, zinc electrode and GF/A separator before and after cycling in KOH system. (i) Optical image comparison of the Sn collector, zinc electrode and gel electrolyte before and after cycling in AG system.

Supplementary Figure S34

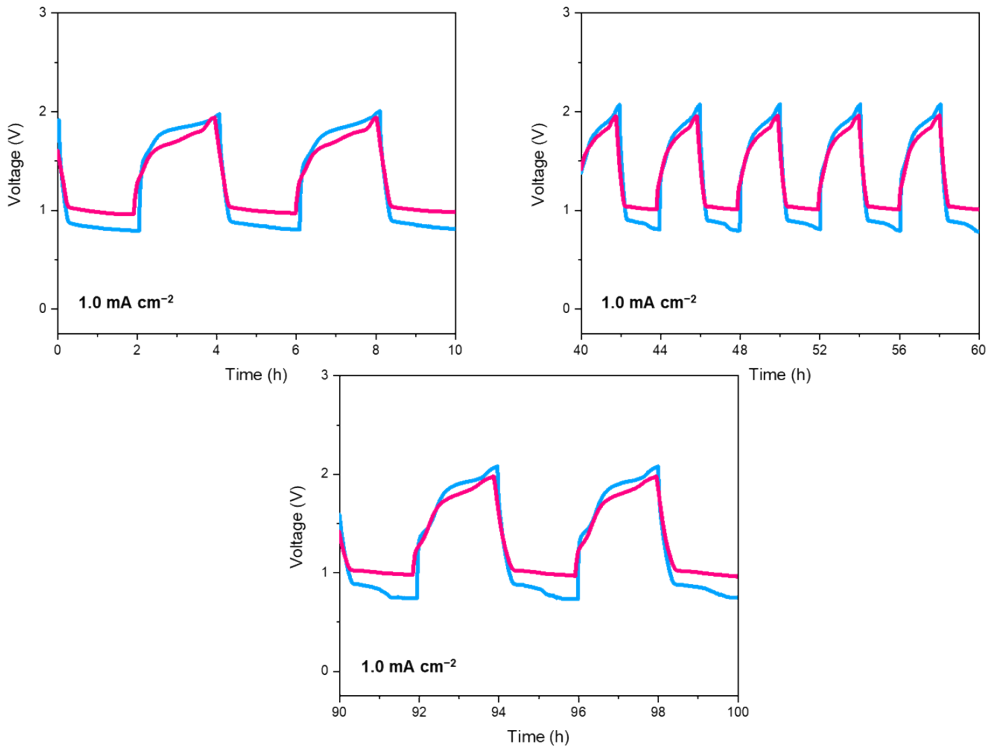

Supplementary Figure S34. Comparison of galvanostatic cycling charge and discharge of zinc-air batteries based on liquid (bule) and AG (red) electrolyte.

Supplementary Figure S35

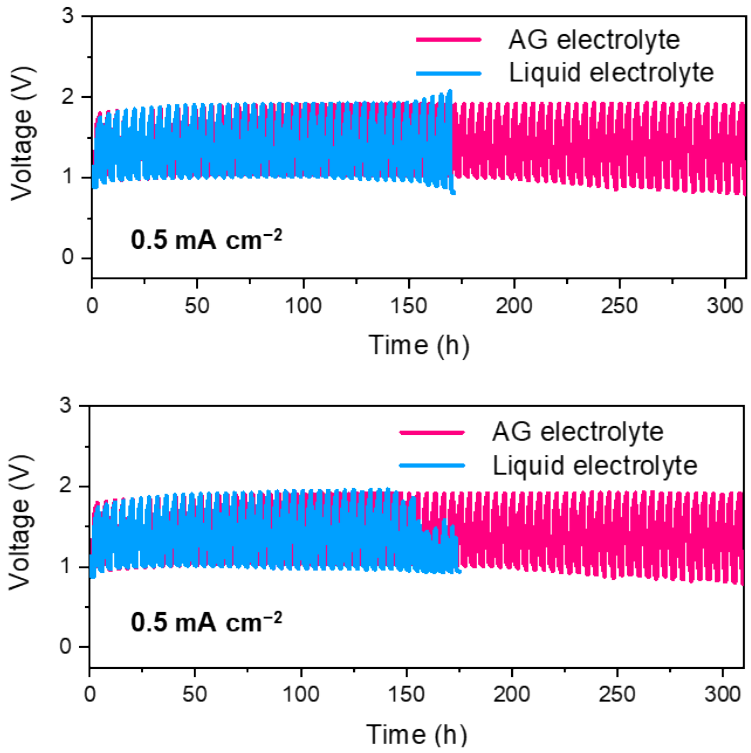

Supplementary Figure S35. Cycling charge-discharge comparison of zinc-air batteries assembled with liquid and AG electrolytes at a current density of 0.5 mA cm^{-2}.

Supplementary Figure S36

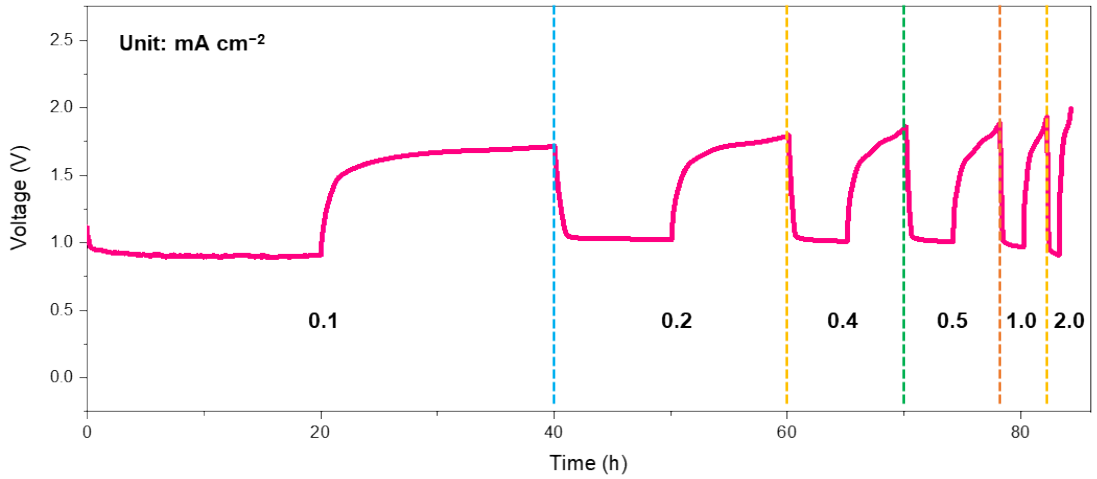

Supplementary Figure S36. Galvanostatic cycle profiles of the zinc-air batteries in a capacity fixed mode (fixed capacity: 2.0 mAh cm^{-2}) at 0.1, 0.2, 0.4, 0.5, 1.0, and 2.0 mA cm^{-2}.

Supplementary Figure S37

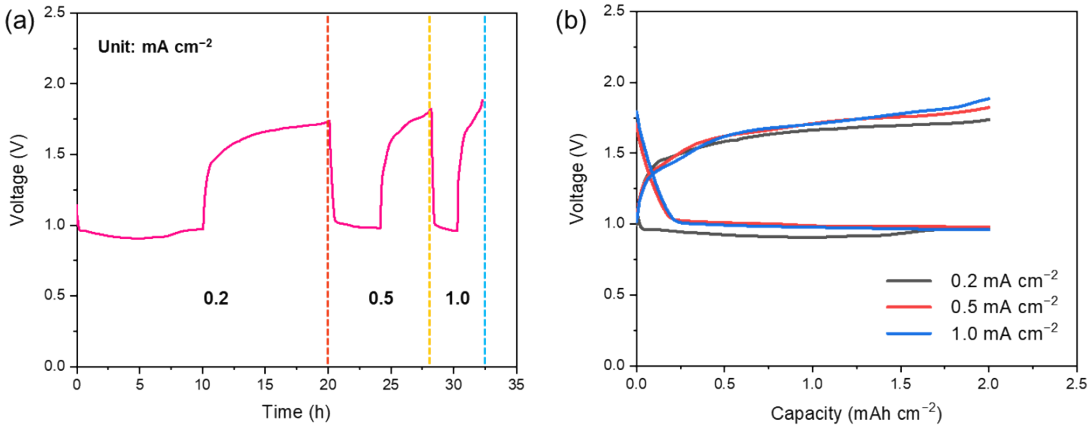

Supplementary Figure S37. Galvanostatic (a) cycle and (b) voltage profiles of the zinc-air batteries in a capacity fixed mode (fixed capacity: 2.0 mAh cm^{-2}) at 0.2, 0.5, and 1.0 mA cm^{-2}.

Supplementary Figure S38

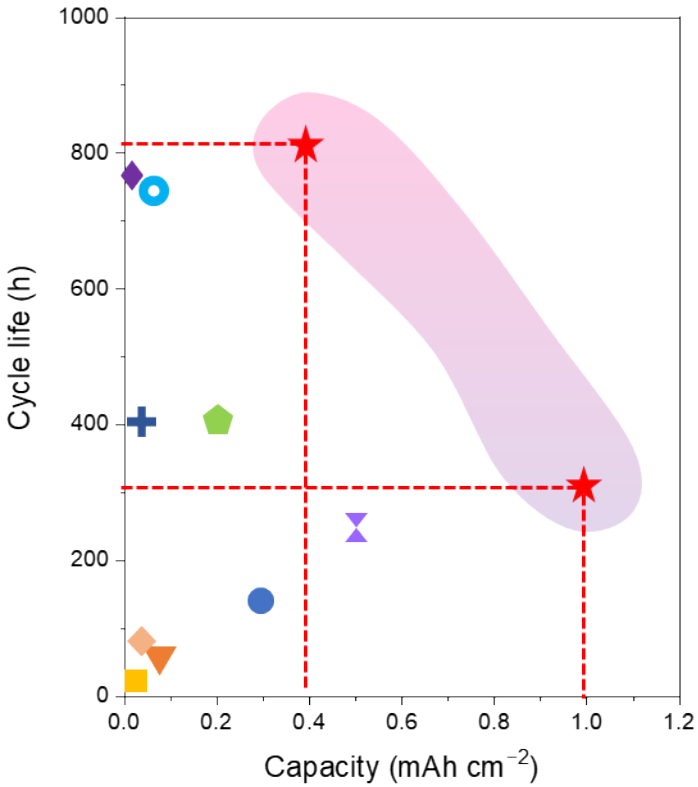

Supplementary Figure S38. The comparison of cycle life with previously reported zinc-air batteries.

Supplementary Figure S39

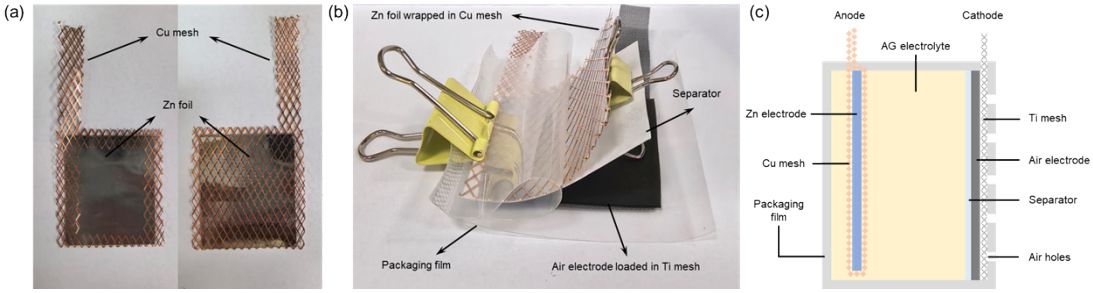

Supplementary Figure S39. (a) Physical images of zinc foil wrapped in Cu mesh. (b) Structural composition of pouch battery. (c) Schematic diagram of the structure of zinc-air pouch battery.

Supplementary Figure S40

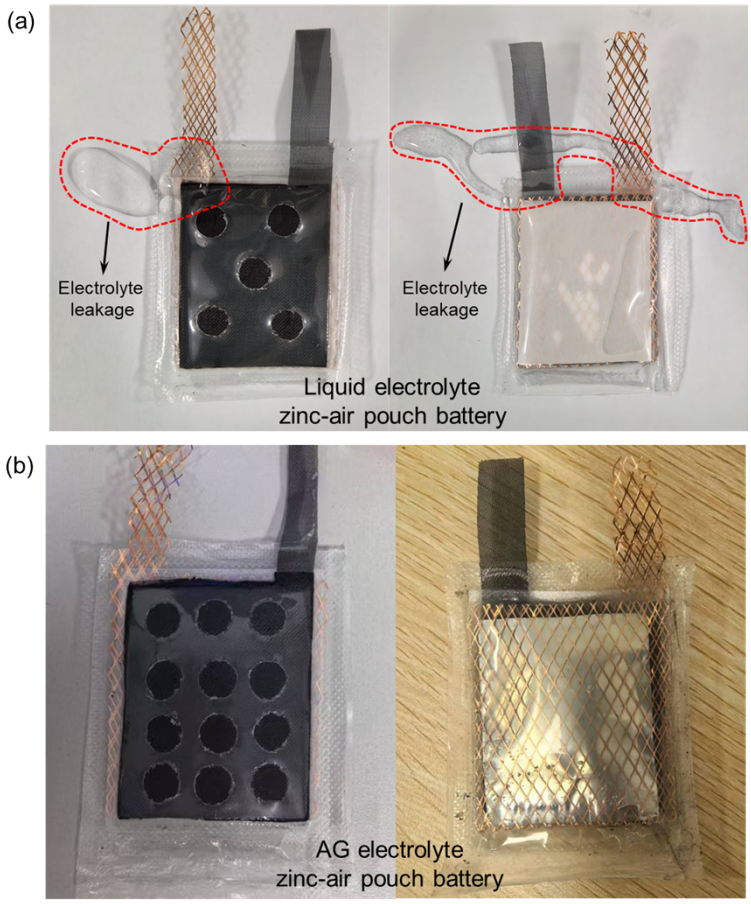

Supplementary Figure S40. The physical picture of the zinc-air pouch battery assembled with (a) liquid electrolyte and (b) AG electrolyte.

Supplementary Figure S41

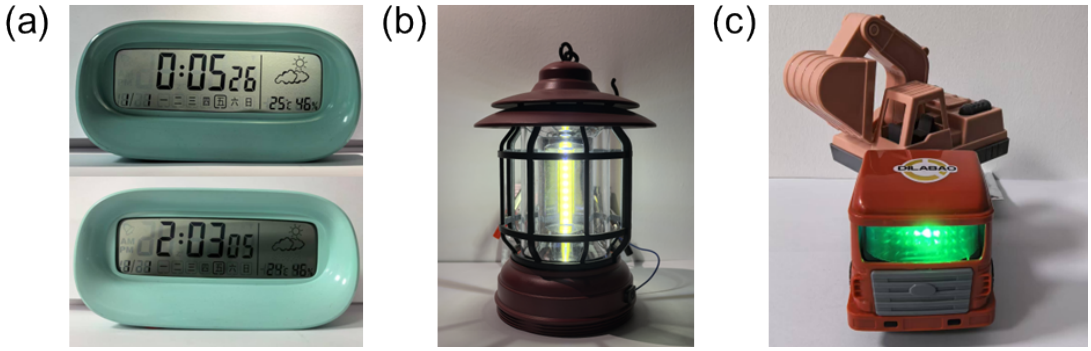

Supplementary Figure S41. Practical applications of AG-based zinc-air pouch batteries: (a) activating the electronic clock, (b) supplying power to lighting lamp and (c) driving the toy car.

Supplementary Figure S42

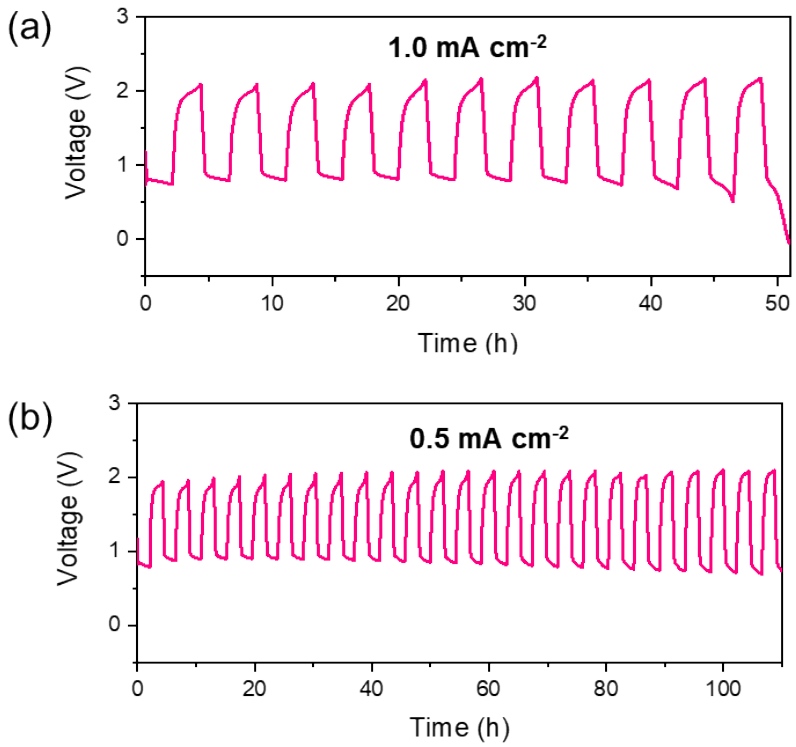

Supplementary Figure 42. Galvanostatic cycle profiles of the zinc-air pouch battery at the current density of 1.0 mA cm^{-2} (1.0 mAh cm^{-2}) (a) and 0.5 mA cm^{-2} (0.5 mAh cm^{-2}) (b).

Supplementary Figure S43

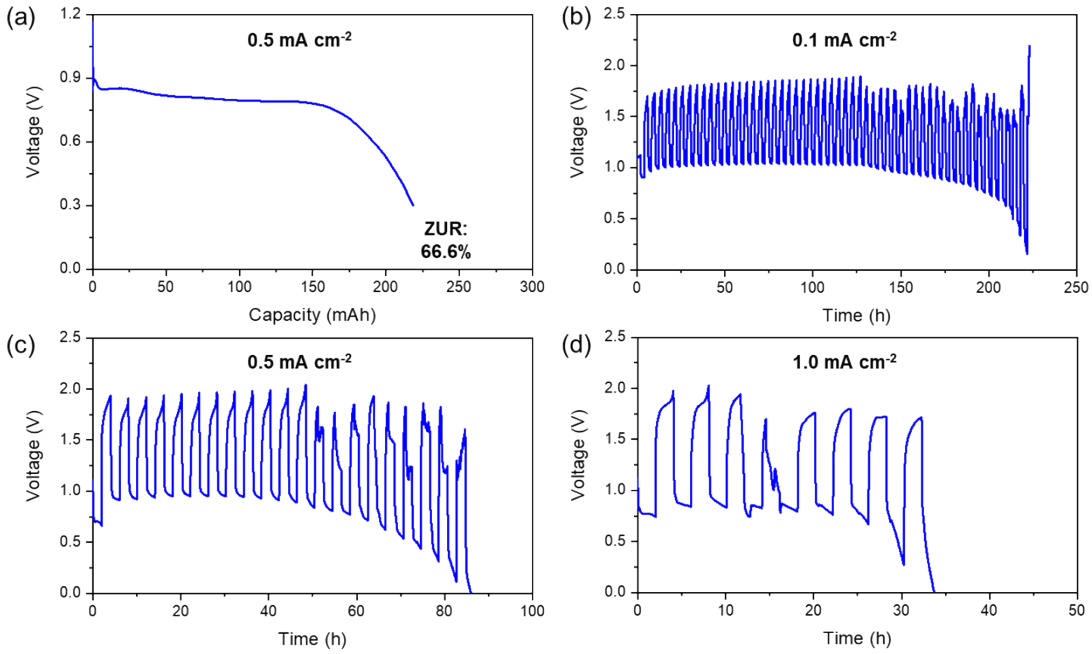

Supplementary Figure S43. (a) Galvanostatic discharge profile of zinc-air pouch battery based on liquid electrolyte at 0.5 mA cm^{-2}. Cycling performance of the zinc-air pouch battery based on liquid electrolyte at a current density of 0.1 mA cm^{-2} (b), 0.5 mA cm^{-2} (c), 1.0 mA cm^{-2} (d).

Supplementary Table S1. The comparison of ionic conductivity with previously reported gel electrolytes.

Gel electrolyte	Monomer	Solution	Ionic conductivity (mS cm^{-1})	Ref.
AG	Agar	0.3 M $Zn(OTf)_2$	21.0	This work
PB-CPEs	PVA	1.0 M $Zn(OTf)_2$	16.3	1
ZS/GL/AN	Glycerol + Acetonitrile	3.0 M $ZnSO_4$	13.94	2
Phos-XK	Xanthan gum Konjac glucomannan	2.0 M $ZnSO_4$	20.72	3
PSX	PVA/DMSO + Xanthan gum	2.0 M $ZnSO_4$	18.86	4
PAM + 45% Tre	Trehalose + PAM	2.0 M $ZnSO_4$	10.98	5
SLA	PEG-Zn^{2+}/Carbon	2.0 M $Zn(ClO_4)_2$	12.6	6
CSAM-C	Carboxymethyl chitosan PAM	2.0 M $Zn(ClO_4)_2$	7.8	7
PZIB	3-(1-vinyl-3-imidazolio) propanesulfonate/ Bacterial cellulose	2.0 M $ZnSO_4$ 0.1 M $MnSO_4$	21.88	8
W2HE	PAM	2.0 M $ZnSO_4$ 0.1 M $MnSO_4$	3.93	9
ZIG	1-vinylimidazole Acetonitrile 1,3-propanesultone	$Zn(TFSI)_2$	2.6	10

Supplementary Table S2. The comparison of cycle life with previously reported zinc-air batteries.

Type	Current density (mA cm^{-2})	Capacity (mAh cm^{-2})	Cycle life (h)	Ref.
AG-ZAB	0.2	0.4	810	This work
	0.5	1.0	300	This work
Alkaline ZAB	0.5	0.25	136	11
	1.5	0.01	12	12
	0.5	0.083	40	13
	0.1	0.033	64	14
Non-alkaline ZAB	0.2	0.2	400	15
	0.1	1.0	600	16
	0.1	0.017	770	17
	0.4	1.0	500	18
	0.1	0.05	773	19
	0.1	0.05	400	20
	0.1	0.017	900	21
	1.0	0.5	250	22

References

[1] Zheng Q, Liu L, Hu Z, *et al*., Altering the Zn^{2+} Migration Mechanism Enables the Composite Hydrogel Electrolytes with High Zn^{2+} Conduction and Superior Anti-Dehydration, *Adv. Funct. Mater.*, 2025, **35**, 2504782.

[2] Wei T, Ren Y, Li Z, *et al*., Bonding interaction regulation in hydrogel electrolyte enable dendrite-free aqueous zinc-ion batteries from −20 to 60 ℃, *Chem. Eng. J.*, 2022, **434**, 134646.

[3] Gou L, Zhu L, Wang W, *et al.*, From Physical Cross-Linking to Tailored Phosphorylation: Unlocking High-Performance and Biocompatible Xanthan-Konjac Hydrogels for Zinc-Ion Batteries, *Adv. Mater.*, 2025, **37**, 2505132.

[4] Fu C, Wang Y, Lu C, *et al.*, Modulation of hydrogel electrolyte enabling stable zinc metal anode, *Energy Storage Materials*, 2022, **51**, 588-598.

[5] Yang S, Wu Q, Li Y, *et al.*, A Bio-Inspired Multifunctional Hydrogel Network with Toughly Interfacial Chemistry for Dendrite-Free Flexible Zinc Ion Battery, *Angew. Chem., Int. Ed.,* 2024, **136**,44, e202409160.

[6] Liu Q, Yu Z, Zhou R, *et al.*, A semi-liquid electrode toward stable Zn powder anode, *Adv. Funct. Mater.*, 2023, **33**, 5, 2210290.

[7] Huang S, Hou L, Li T, *et al.*, Antifreezing hydrogel electrolyte with ternary hydrogen bonding for high-performance zinc-ion batteries, *Adv. Mater.*, 2022, **34**, 14, 2110140.

[8] Hao Y, Feng D, Hou L, *et al.*, Gel electrolyte constructing Zn (002) deposition crystal plane toward highly stable Zn anode, *Adv. Sci.*, 2022, **9**,7, 2104832.

[9] He Q, Chang Z, Zhong Y, *et al.*, Highly entangled hydrogel enables stable zinc metal batteries via interfacial confinement effect, *ACS Energy Lett.*, 2023, **8**, 12, 5253-5263.

[10] Wang, Y., Li, Q., Hong, H. *et al.*, Lean-water hydrogel electrolyte for zinc ion batteries, *Nat. Commun.*, 2023, **14**, 3890.

[11] Cui Y, Zhu Y, Du J, *et al.*, A high-voltage and stable zinc-air battery enabled by dual-hydrophobic-induced proton shuttle shielding, *Joule*, 2022, **6**, 7, 1617-1631.

[12] Fan K, Li Z, Song Y, *et al.*, Confinement synthesis based on layered double hydroxides: a new strategy to construct single-atom-containing integrated electrodes, *Adv. Funct. Mater.*, 2021, **31**,10, 2008064.

[13] Yang Z, Li P, Li J, *et al.*, All-in-One Polymer Gel Electrolyte towards High-Efficiency and Stable Fiber Zinc-Air Battery, *Angew. Chem., Int. Ed.,* 2025, **137**, 2, e202414772.

[14] Zhu D, Zhao Q, Fan G, *et al.*, Photoinduced oxygen reduction reaction boosts the output voltage of a zinc-air battery, *Angew. Chem., Int. Ed.,* 2019, **131**, 36, 12590-12594.

[15] Zhang W, Zhang J, Wang N, *et al.*, Two-electron redox chemistry via single-atom catalyst for reversible zinc-air batteries, *Nat. Sustain.*, 2024, **7**, 4, 463-473.

[16] Sun W, Küpers V, Wang F, *et al.*, A non-alkaline electrolyte for electrically rechargeable zinc-air batteries with long-term operation stability in ambient air, *Angew. Chem., Int. Ed.,* 2022, **61**, 38, e202207353.

[17] Fan X, Xie Y, Jiao Y, *et al.*, Monodentate acetate anion enhanced hydrogel electrolyte for long-term lifespan Zn-air batteries, *ACS Nano*, 2024, **18**, 52, 35705-35717.

[18] Liao X, Chen S, Chen J, *et al.*, Suppressing Zn pulverization with three-dimensional inert-cation diversion dam for long-life Zn metal batteries, *Proc. Natl. Acad. Sci.*, 2024, **121**, 8, e2317796121.

[19] Li H, Xu F, Lin X, *et al.*, Self-Healing Ionogel with Unprecedented High Gel-Sol Transition Temperature Enables Self-Healing Zinc-Air Battery Operation at 100 ℃, *Adv. Funct. Mater.*, 2025, e13459.
[20] Li H, Xu F, Li Y, *et al.*, Self-healing ionogel-enabled self-healing and wide-temperature flexible zinc-air batteries with ultra-long cycling lives, *Adv. Sci.*, 2024, **11**, 25, 2402193.
[21] Liu X, Wang J, Lv P, *et al.*, Gel polymer electrolyte based on deep eutectic solvent in flexible Zn-air batteries enables dendrite-free Zn anode, *Energy Storage Materials*, 2024, **69**, 103382.
[22] Zhao C, Guo R, Zhai Y, *et al.*, Promoting Reaction Kinetics of the Air Cathode for Neutral Zinc-Air Batteries by the Photothermal Effect, *ACS Applied Materials & Interfaces*, 2024, **16**, 46, 63580-63588.